

# Parametric Study on a Sinusoidal Riblet for Drag Reduction by Direct Numerical Simulation

M. Sasamori<sup>1</sup> · O. Iihama<sup>1</sup> · H. Mamori<sup>2</sup> · K. Iwamoto<sup>1</sup> ·  
A. Murata<sup>1</sup>

Received: 25 November 2015 / Accepted: 1 March 2017 / Published online: 1 April 2017  
© Springer Science+Business Media Dordrecht 2017

**Abstract** The direct numerical simulation of fully developed turbulent channel flow with a sinusoidal riblet surface has been carried out at the friction Reynolds number of 110. Lateral spacing of adjacent walls in a sinusoidal riblet is varied sinusoidally in the streamwise direction. The average lateral spacing of a sinusoidal riblet is larger than the diameter of a quasi-streamwise vortex and its wetted area is smaller than that of ordinary straight-type riblets. We investigate the effect of sinusoidal riblet design parameters on the drag reduction rate and flow statistics in this paper. The parametric study shows that the maximum total drag reduction rate is approximately 9.8% at a friction Reynolds number of 110. The riblet induces downward and upward flows in the expanded and contracted regions, respectively, which contribute to periodic Reynolds shear stress. However, the random Reynolds shear stress decreases drastically as compared with the flat surface case, resulting in the reduction of total drag owing to the sinusoidal riblet. We also performed vortex tracking to discuss the motion of the vortical structure traveling over the sinusoidal riblet surface. Vortex tracking and probability analysis for the core of the vortical structure show that the vortical structure is attenuated owing to the sinusoidal riblet and follows the characteristic flow. These results show that the high skin-friction region on the channel wall is localized at the expanded region of the riblet walls. In consequence, the wetted area of the riblet decreases, resulting in the drag-reduction effect.

**Keywords** Riblet · Fluid friction · Drag reduction · Turbulent flow · Direct numerical simulation

---

✉ K. Iwamoto  
iwamotok@cc.tuat.ac.jp

<sup>1</sup> Department of Mechanical Systems Engineering, Tokyo University of Agriculture and Technology, 2-24-16 Nakacho, Koganei-shi, Tokyo 184-8588, Japan

<sup>2</sup> Department of Mechanical Engineering, Tokyo University of Science, 6-3-1 Nijjuku, Katsushika, Tokyo 125-8585, Japan

## 1 Introduction

Skin-friction drag increases significantly in wall turbulence, which raises the energy costs of transportation equipment, and techniques for reducing skin-friction drag are of importance in various engineering fields. To utilize skin-friction drag reduction techniques in real situations, some practical difficulties arise, e.g., technical problems or cost restrictions. A micro-grooved riblet surface is known to reduce skin friction in wall turbulence and is easy to adopt in existing equipment. Riblet surfaces, therefore, are believed to be one of the most promising methods for practical applications. Today there are two types of the riblet: a two-dimensional (2-D) riblet and a three-dimensional (3-D) riblet. The former and latter indicate that the riblet has a shape that is either constant or that varies in the streamwise direction, respectively.

As for the 2-D riblet surface, Walsh [1] pioneered systematic investigation of triangular and scalloped riblet surfaces. They obtained a friction drag reduction of up to 8% when the lateral spacing of the adjacent riblet walls was less than 25 viscous units. Since then, many studies have been performed under various flow conditions (e.g., [2–5]) and clarified that 2-D riblets achieve maximum drag reduction at a size near  $s^+ \approx 15$ . In particular, Bechert et al. [2] furthered riblet research experimentally and optimized the shape of “blade riblets,” which involve very thin adjacent riblet walls along the streamwise direction. They confirmed a drag reduction rate of approximately 10% on the blade riblet surface.

The drag reduction mechanism of 2-D riblets has also been discussed. Bechert et al. [6] pointed out that the decrement of the spanwise velocity fluctuation in the region near the riblet surface contributes to drag reduction. They also introduced a concept of “protrusion height,” which is the distance between a riblet’s tip and the virtual origin of the velocity profile. Luchini et al. [7] discussed a relationship between the drag reduction effect and the protrusion height quantitatively. Garcia-Mayoral and Jimenez [8] performed direct numerical simulation (hereafter referred to as DNS) to explain why the viscous region, in which the drag reduction due to the 2-D riblet varies linearly with the lateral spacing of the riblet, breaks down over a 2-D riblet. Lee and Lee [9] and Suzuki et al. [10] performed particle tracking velocimetry (PTV) measurements over a v-groove riblet surface and concluded that attenuation of the splatting phenomenon causes a decrease of quasi-streamwise vortex regeneration. Choi et al. [11] performed DNS for a fully developed turbulent channel flow with a 2-D riblet surface. They reported drag-reducing riblets decrease the root mean square (RMS) velocity fluctuations near the riblets and discussed the relation between the drag reduction and vortical structures. The riblet affects ejection and sweep events and inhibits quasi-streamwise vortices in the region near the wall because the lateral spacing of the adjacent riblet walls is smaller than the diameter of the quasi-streamwise vortices. Chu and Karniadakis [12] and Goldstein [13] also confirmed the decreasing RMS near the riblets by prohibiting larger scales of turbulence from interacting with much of the riblet surface area, resulting in decreasing high shear stress regions.

As for practical applications, a 2-D riblet surface was installed on a commercial aircraft and a decrease of 2% in total drag was confirmed, e.g., as reviewed in [14]; however, the decrease in fuel costs owing to the drag reduction effect was not sufficient to cover the maintenance costs of the riblet. Therefore, a riblet surface that produces a larger drag reduction effect is required.

In contrast to 2-D riblet surfaces, 3-D riblets have also been investigated in order to obtain larger drag reduction, e.g., by mimicking shark skin [15], wavy shapes [16, 17], and herringbone shapes [18]. Peet et al. [16] conducted large eddy simulations (LES) of channel flows with wavy riblet shapes that mimic the spanwise oscillation technique, e.g., [19–23].

They observed a decrease in wall-normalized and spanwise velocity fluctuations and obtained a maximum drag-reduction of 14%. However, drag reduction using 3-D riblets is comparable to that using optimized 2-D riblets because optimization for 3-D riblets is difficult owing to their many design parameters.

As one of the investigations into 3-D riblets, our research group has proposed a sinusoidal riblet surface. The lateral spacing of a sinusoidal riblet's adjacent walls varies sinusoidally in the streamwise direction so that its averaged lateral spacing is larger than that of a typical 2-D riblet and the diameter of a quasi-streamwise vortex. Thus, the wetted area of the sinusoidal riblet surface is smaller than that of other 2-D and 3-D riblets. Major difference between the present sinusoidal riblet surface and the ordinary wavy riblet [16, 17] is phase relationship between adjacent walls. Because walls of the present sinusoidal riblet are out-of-phase, the induced spanwise velocity is small and the spanwise average should be zero (described below). In contrast, walls of the wavy riblet are in-phase and the spanwise velocity plays important role for the skin-friction drag reduction. Therefore, the drag reduction mechanism in the sinusoidal riblet surface is expected to be different from the wavy wall riblet. Sasamori et al. [24] performed an experimental study of a sinusoidal riblet surface in a turbulent channel flow and confirmed a drag reduction of 11.7%. Their two-dimensional PIV measurement indicates the drag reduction mechanism: the sinusoidal riblet surface induces downward and upward flows which prevent vortices from hitting the bottom wall. This results in the significant drag-reduction effect. Yamaguchi et al. [25, 26] also conducted an experimental study using dual-plane stereoscopic particle image velocimetry (DPS-PIV) measurement. Since all velocity components can be measured by the DPS-PIV and an instantaneous velocity deformation tensor can be obtained, vortical structures can be identified by using a second invariant of the tensor (the so-called  $Q$  value). They revealed that the riblet degrades vortical structures and that its advection velocity is the same as that of the induced flow when using a sinusoidal riblet in the wall-normal direction.

In this study, direct numerical simulation (DNS) of turbulent flows over a sinusoidal riblet surface is done as an extension of previous studies [24–26]. We perform a parametric study to investigate the effect of sinusoidal riblet design parameters on the drag reduction rate. Moreover, we discuss advection of vortical structures three-dimensionally to clarify the drag reduction mechanism. The results are expected to potentially lead to designing riblet configurations which give even larger drag reduction.

The structure of this paper is as follows. The numerical conditions are described in Section 2. Section 3 describes the drag reduction effect of the sinusoidal riblet. Section 4 shows mean flows on the sinusoidal riblet. Section 5 shows results of the parametric study. We discuss the drag reduction mechanism in Section 6 and give our conclusions in Section 7.

## 2 Numerical Method

DNS is conducted for fully developed turbulent channel flow with the sinusoidal riblet surface. The computational conditions are summarized in Table 1. The computational grid size is uniform in homogeneous directions and is non-uniform in the wall-normal direction. We provide five computational domains: “reference” domain is mainly used in this paper; “x-fine”, “y-fine”, and “z-fine” domains have fine computational mesh in the streamwise, wall-normal, and spanwise directions, respectively; “large” domain has large computational domain. A periodic condition is imposed in homogeneous directions while a no-slip condition is imposed on the channel walls and the riblet surface. The mean pressure gradient is kept constant. A friction Reynolds number, defined by a friction velocity in the flat-surface

**Table 1** Numerical condition

Domain	$Re_\tau$	$L_x \times L_y \times L_z$	$N_x \times N_y \times N_z$	$\Delta x^+ \times \Delta y^+ \times \Delta z^+$
Reference	110	$1.25\pi\delta \times 2\delta \times 0.5\pi\delta$	$192 \times 216 \times 192$	$2.25 \times (0.3 - 2.8) \times 0.89$
x-fine	110	$1.25\pi\delta \times 2\delta \times 0.5\pi\delta$	$384 \times 216 \times 192$	$1.125 \times (0.3 - 2.8) \times 0.89$
y-fine	110	$1.25\pi\delta \times 2\delta \times 0.5\pi\delta$	$192 \times 432 \times 192$	$2.25 \times (0.15 - 1.4) \times 0.89$
z-fine	110	$1.25\pi\delta \times 2\delta \times 0.5\pi\delta$	$192 \times 216 \times 576$	$2.25 \times (0.3 - 2.8) \times 0.29$
Large	110	$5\pi\delta \times 2\delta \times 2\pi\delta$	$768 \times 216 \times 768$	$2.25 \times (0.3 - 2.8) \times 0.89$

case  $u_\tau$ , flat and the channel half-width  $\delta$ , is set to be  $Re_\tau = 110$ . The pressure gradient is adjusted so that the friction Reynolds number in all cases is the same precisely. The friction velocity is calculated by  $u_{\tau, flat} = (\tau_w/\rho)^{1/2}$  where  $\tau_w$  is the mean wall shear of the flat channel and  $\rho$  is the density. The plus sign superscript indicates wall units in the following discussion.

The governing equations include the incompressible continuity and Navier-Stokes equations. These equations are spatially discretized using the finite-difference method with a second-order central differencing scheme. As for the time steps, the second-order Crank-Nicolson scheme is employed for the viscous term in the wall-normal direction and the low-storage third-order Runge-Kutta scheme is employed for the other terms. The simplified marker and cell (SMAC) method is adopted for velocity-pressure coupling. The Poisson equation of pressure is solved by using a fast Fourier transform in the homogeneous directions and a tri-diagonal matrix algorithm in the wall-normal direction.

Figure 1 shows the channel flow with a sinusoidal riblet surface of the reference shape. The velocities are denoted by  $u$ ,  $v$ , and  $w$  in the  $x$ -,  $y$ -, and  $z$ -directions, respectively. Both upper and lower walls are riblet-surfaced. The riblet is represented by using an immersed boundary method [27], and the sinusoidal riblets have rectangular cross sections. The riblets have five parameters: the height of the riblet wall,  $h^+$ ; thickness of the riblet wall,  $t^+$ ; wavelength of the sinusoidal wave,  $\lambda^+$ ; amplitude of the wave,  $a^+$ ; and averaged lateral spacing,  $s_{ave}^+$ . Parameter sets are summarized in Table 2 and twelve cases with the reference domain are investigated in this study. If the amplitude is zero, the riblet walls are straight in the streamwise direction and its averaged lateral spacing is 42.27 in the wall unit. The parameter set of  $t^+ = 1.8$ ,  $h^+ = 7.5$ ,  $a^+ = 14.22$ ,  $\lambda^+ = 431.6$ , and  $s_{ave}^+ = 42.27$  is chosen as the reference shape. Note that the average lateral spacing of the adjacent walls of the riblet  $s_{ave}^+$  is kept constant and the wavelength is determined based on the streamwise length of the computational domain.

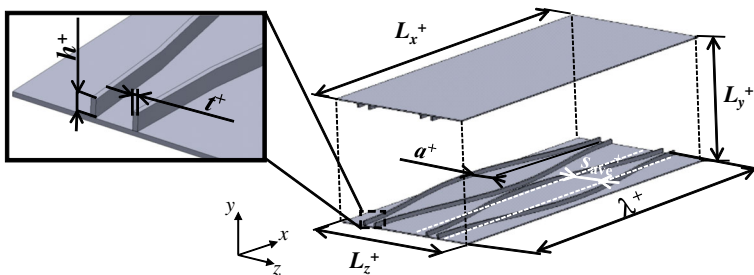


**Fig. 1** Computational domain of the channel flow and the sinusoidal riblet surface

**Table 2** Parameter sets for the sinusoidal riblet

	$h^+$	$t^+$	$a^+$	$\lambda^+$	$s_{ave}^+$	$R_D[\%]$
Reference shape	7.5	1.8	14.22	431.6	42.27	8.7
Case 1	7.5	3.6	14.22	431.6	42.27	6.5
Case 2	7.5	5.4	14.22	431.6	42.27	6.2
Case 3	3.75	1.8	14.22	431.6	42.27	5.7
Case 4	6	1.8	14.22	431.6	42.27	8.2
Case 5	8.5	1.8	14.22	431.6	42.27	4.5
Case 6	7.5	1.8	0	431.6	42.27	4.3
Case 7	7.5	1.8	7.1	431.6	42.27	6.7
Case 8	7.5	1.8	15.63	431.6	42.27	9.8
Case 9	7.5	1.8	18.47	431.6	42.27	6.9
Case 10	7.5	1.8	14.21	107.9	42.27	-11.9
Case 11	7.5	1.8	14.21	215.8	42.27	-0.2

The friction Reynolds number is 110 in all cases with the reference domain

Here the present riblets in the reference shape are compared with the optimized 2-D riblet [2]:

- the thickness,  $t_{3-D}^+/t_{2-D}^+ \approx 5$ ;
- the height of the riblet,  $h_{x,3-D}^+/h_{x,2-D}^+ \approx 0.83$ ;
- the mean lateral spacing,  $s_{3-D}^+/s_{2-D}^+ \approx 2.3$ ;
- the wetted area,  $A_{3-D}^+/A_{2-D}^+ \approx 0.66$ .

The subscripts ‘2-D’ and ‘3-D’ indicate 2-D and 3-D riblets, respectively. Note that the wetted area  $A$  of the sinusoidal riblet is 0.66 times smaller than that of the optimized 2-D riblet. This is because the wall shape of the sinusoidal riblet is not straight in the streamwise direction, where the number of sinusoidal riblet walls decreases.

Subsequently, comparison with a wavy riblet [16] is discussed. The adjacent walls of the wavy riblet are in-phase so that its lateral spacing is uniform. The skin-friction drag reduction is up to 14% for the parameter set for height  $h^+ = 8$ , lateral spacing  $s^+ = 16$ , amplitude  $a^+ = 28$ , and streamwise wavelength  $\lambda^+ = 1080$ . Peet et al. [16] concluded that the wavelength of  $\lambda^+ \geq 1080$  is effective for decreasing the skin-friction drag. In contrast, the wavelength of the present sinusoidal riblet is much shorter than that of the wavy riblet while drag reduction is still obtained (as shown later). For the other parameters, the height is comparable, the averaged lateral spacing is small, and the amplitude is approximately half as compared with the wavy riblet. Note that the averaged lateral spacing of the present riblet is larger than not only that of the wavy riblet but also compared with the diameter of quasi-streamwise vortices.

The present DNS is conducted at the very low Reynolds number of  $Re_\tau = 110$ . Spalart and McLean [28] derived the formula which indicates that the drag reduction effect decreases as increasing the Reynolds number if the mean streamwise velocity shift is fixed for a given riblet type. We expect, however, to observe a drag reduction effect due to the present riblet in the higher Reynolds numbers because the present riblet decreases turbulence in the region near the walls. There is an implicit formula [29] which indicates that the drag reduction only slightly decreases at high Reynolds numbers if turbulence

is completely damped in the region near the wall. For example, consider a drag reduction of 43% at  $Re_\tau = 10^3$  and 35% even at  $Re_\tau = 10^5$ , when turbulence only vanishes below  $y^+ < 10$ . Additionally, Garcia-Mayoral and Jimenez [30] made the DNS of the turbulent channel flow with the 2-D riblet surface. They compared the drag reduction rate of the flows at  $Re_\tau = 550$  and  $Re_\tau = 180$  and they reported that the difference in the drag reduction rate between them is small. Accordingly, the Reynolds number dependency of the drag reduction rate is small and the drag reduction effect is expected at high Reynolds number flows.

Here, the verification for the present DNS is discussed. Figure 2 shows the mean streamwise velocity, the rms value of velocity fluctuation, and the Reynolds shear stress of the flat surface case at friction Reynolds number of 110 in the reference domain, together with the DNS data [31]. The mean streamwise velocity and the RSS profiles in the present simulation agree with the DNS data. On the other hand, the RMS profiles do not agree with the DNS data. This is because the small computational domain.

Figure 3a and b shows dependency of the grid resolution for the flat and riblet cases: the mean streamwise velocity and the RSS in the “reference”, “x-fine”, “y-fine”, and “z-fine” are shown. In the viscous sublayer and buffer layer, the mean streamwise velocity computed in the finer resolution case shows good agreement with that computed in the reference case, but the slight difference remains in logarithmic layer. Since the effect of the riblet appears near the wall region (viscous sublayer and buffer layer), we think that the resolution in the reference case is enough to relatively evaluate the flow over the riblet surface. Although there are slight differences, we observed the similar trend: the mean streamwise velocity  $\langle \overline{u^+} \rangle$  of the riblet case decreases in the viscous sublayer and it increases in the buffer layer,

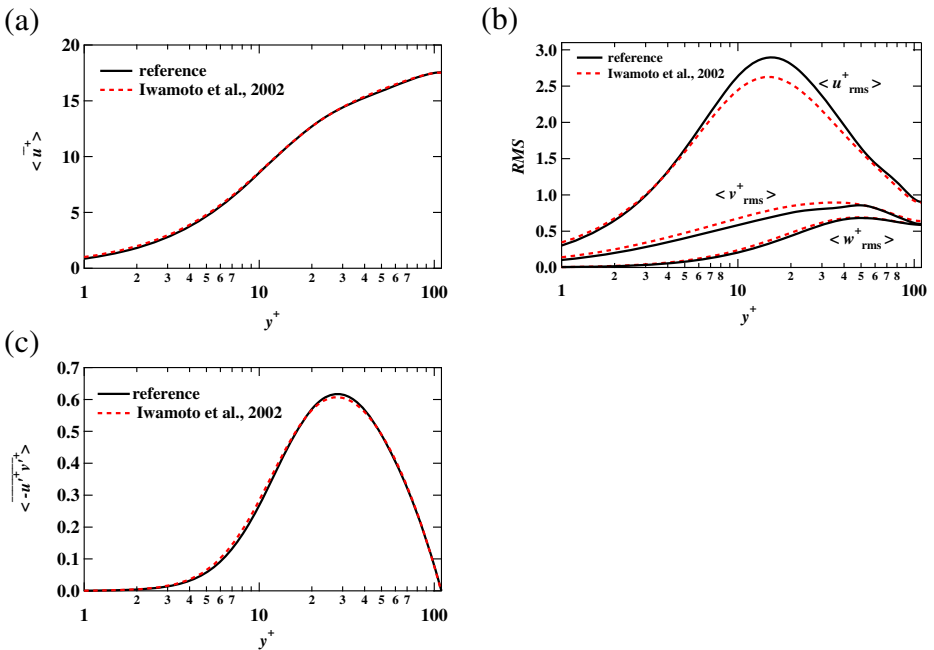


**Fig. 2** Comparison of statistics in the flat case: (a) the mean streamwise velocity, (b) the RMS value, (c) the Reynolds shear stress. The *solid and broken lines* show the present DNS in the reference domain and the DNS database [31], respectively

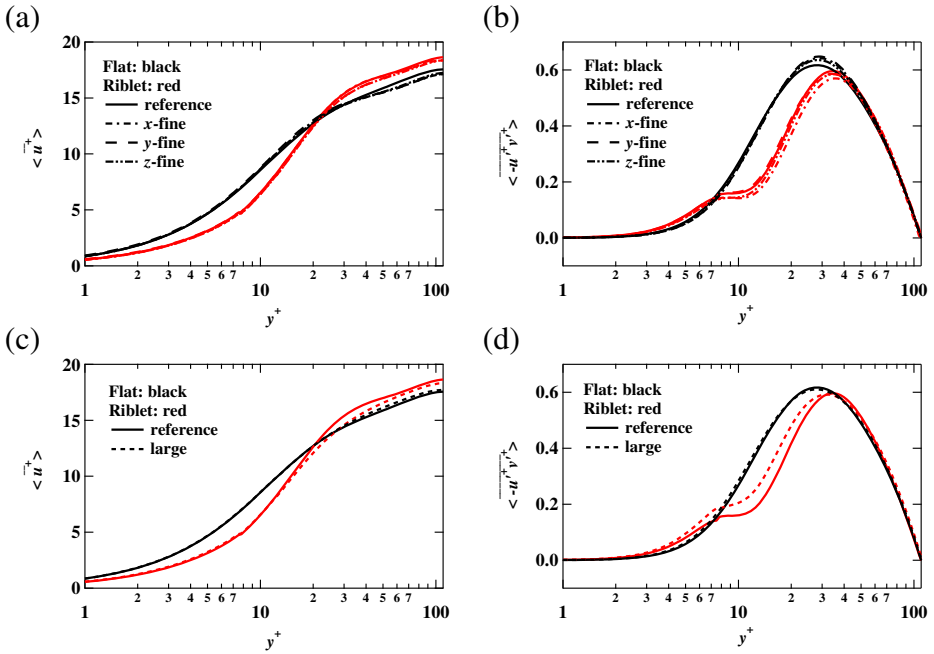


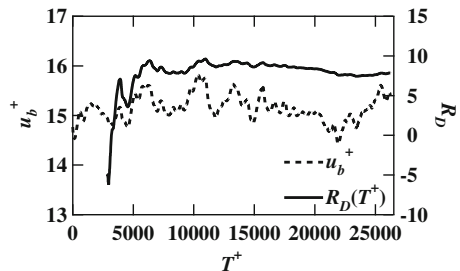
**Fig. 3** Comparison of the mean streamwise velocity and the RSS: (a) and (b), for different resolution; (c) and (d), for different domain size. The riblet is the reference shape

as compared with that of the flat case; the RSS of the riblet case decreases below that of the flat case at  $y^+ > 10$ . Figure 3c and d shows dependency of the computational domain size (i.e., comparison between the “reference” and “large” domains) and the similar trend observed in Fig. 3a and b is also obtained. The drag reduction rate  $R_D$  in the finer grid cases and the large computational domain is slight different (a few percent) from that in the “reference” case. Therefore, we use the reference domain in this paper and make discussion as relative comparison for different design parameter cases.

### 3 Drag Reduction Effect

Figure 4 shows the time trace of the bulk velocity in the reference computational domain with the reference riblet shape. Although its computation time is long, the bulk velocity

**Fig. 4** Time evolution of bulk velocity and total drag reduction  $R_D$  on the reference sinusoidal riblet



varies in time and it does not show the steady state. It is due to the small computational domain. Accordingly, we define the drag reduction which is a function of the time  $R_D(T)$  as

$$R_D(T) = \frac{C_{T, f} - C_{T, r}(T)}{C_{T, f}}, \tag{1}$$

Here  $C_T$  means the total drag coefficient and the subscripts f and r denote values for the flat and riblet surfaces, respectively. The total drag coefficient  $C_T$  defined as

$$C_T(T) = \frac{\overline{D_{wall}}(T)}{\frac{1}{2}\rho\overline{U_b}(T)^2}, \tag{2}$$

The averaged wall drag  $D_{wall}$  (i.e., sum of the wall shear stress and pressure drag) and the averaged bulk velocity  $U_b$  are

$$\overline{D_{wall}}(T) = \frac{1}{(T - T_s)} \int_{T_s}^T D_{wall}(T) dT, \tag{3}$$

$$\overline{U_b}(T) = \frac{1}{(T - T_s)} \int_{T_s}^T u_b(T) dT. \tag{4}$$

The time averaging starts at  $T_s^+ = 3000$  since the bulk velocity  $u_b$  is in the transient states at  $0 < T^+ < 3000$ . The  $C_{T, f}$  equals to the skin-friction drag coefficient  $C_{f, f}$ .

The wall drag  $D_{wall}$  is calculated from the momentum balance including the unsteady term as

$$\rho \frac{1}{(T - T_s)} \int_V \int_{T_s}^t \frac{\partial u_b}{\partial T} dT dv = \int_V \left( \frac{\partial P}{\partial x} \right) dv - \int_{S_w} \overline{D_{wall}} ds, \tag{5}$$

where  $T$  and  $\frac{\partial P}{\partial x}$  are time and the mean pressure gradient. The volume and the wetted area of the computational domain except the riblet walls are denoted by  $V$  and  $S_w$ , respectively. These elements are  $dv$  and  $ds$ , respectively. The LHS of Eq. 5 is the unsteady term and the first and second terms in the RHS are contributions from the mean pressure gradient and wall shear stress, respectively. Figure 4 also shows the drag reduction rate  $R_D(T^+)$ . Even though  $R_D(T^+)$  includes the unsteady effect of the bulk velocity,  $R_D(T^+)$  varies in time, e.g., the  $R_D(T^+ = 12,000) = 8.7\%$  and  $R_D(T^+ = 26,000) = 8\%$ . The difference between the maximum and minimum  $R_D(T^+)$  is about 2% of the time averaged  $R_D(T^+)$  and we admit  $\pm 2\%$  of  $R_D(T^+)$  in this paper.

Figure 5 compares flow statistics (the mean streamwise velocity and the RSS) for different averaging time. The averaging times of “reference” and “long time” cases are in

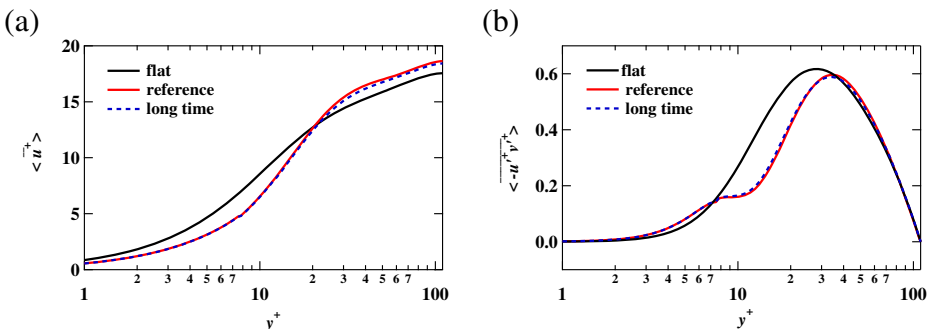


**Fig. 5** Comparison of mean streamwise velocity and the RSS: (a) and (b), for different average time



$5,000 < T^+ < 12,000$  and  $5,000 < T^+ < 26,000$ , respectively. The statistics of the reference case are in good agreement with those of the long time case. Therefore, we have judged that the flow reaches a steady state until  $T^+ = 12,000$  and the paper uses  $R_D(T^+ = 12,000)$  in the parametric study for design parameters of the sinusoidal riblet. Hereafter, we refer the drag reduction rate of  $R_D(T^+)$  by  $R_D$ .

Subsequently, we discuss the accuracy of the immersed boundary method. The riblet wall is expressed by two grids ( $t^+ = 1.8$  and  $\Delta z^+ = 0.89$ ) in the reference domain and the no-slip condition cannot be satisfied only on the corners of the riblet walls by the IBM [27] employed in the present study. Therefore we take priority to satisfy the no-slip condition on the upper surface of the riblet wall over other side walls, since it is particularly important for the drag. As shown in Table 1, the  $z$ -fine domain has large grid number in the spanwise direction where the riblet wall is expressed by the six grids. Because its drag reduction rate is comparable with the reference domain within the error, we concluded that the resolution in the reference domain is enough to express the riblet shape with the IBM.

The drag reductions in all cases are tabulated in Table 2. The drag reduction effect appears in all cases except for the shorter-wavelength Cases 10 ( $\lambda^+ = 107.9$ ) and 11 ( $\lambda^+ = 215.8$ ). The maximum drag reduction is obtained in Case 8 ( $a^+ = 15.63$ ).

The local skin friction and pressure drag coefficients,  $c_f$  and  $c_p$ , are defined as

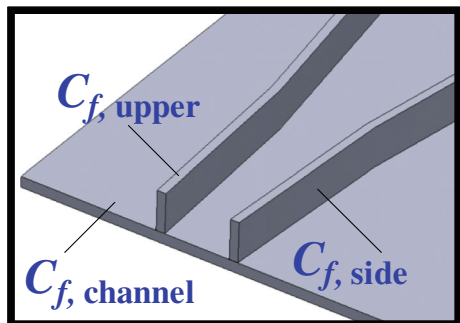
$$c_f = \frac{\tau_{w,x}}{\frac{1}{2}\rho u_b^2}, \tag{6}$$

$$c_p = \frac{p_{w,x}}{\frac{1}{2}\rho u_b^2}, \tag{7}$$

where  $\tau_{w,x}$  and  $p_{w,x}$  are the streamwise components of the shear stress and the pressure on the wall, respectively. Moreover, the local skin friction coefficients  $c_f$  averaged on the channel surface, the riblet upper wall, and the riblet side wall are denoted by  $C_{f, \text{channel}}$ ,  $C_{f, \text{upper}}$ , and  $C_{f, \text{side}}$ , respectively. The components of the riblet surface are shown in Fig. 6. The subscripts “channel,” “upper,” and “side” mean the channel wall, the upper surface of the riblet wall, and the side surface of the riblet wall, respectively. The difference between the total drag (i.e., summation of the drag coefficients  $C_{T,r} = C_{f, \text{channel}} + C_{f, \text{side}} + C_{f, \text{upper}} + C_p$ ) and the driving force for the channel (i.e., the mean pressure gradient) is approximately 5%. This difference rises from the interpolation in the computation of the local wall shear stress and the pressure on the wall, which is displayed as the error bar as shown in Fig. 7.

Figure 7 also shows the contribution ratio to the total drag  $C_T$ . Reduction of net bar height corresponds to the drag reduction. In all cases,  $C_{f, \text{channel}}$  decreases significantly as compared with that of the flat case, while other contributions appear to increase the drag. As

**Fig. 6** Definition of the skin friction drag on the channel wall surface, side and upper surfaces of the riblet wall



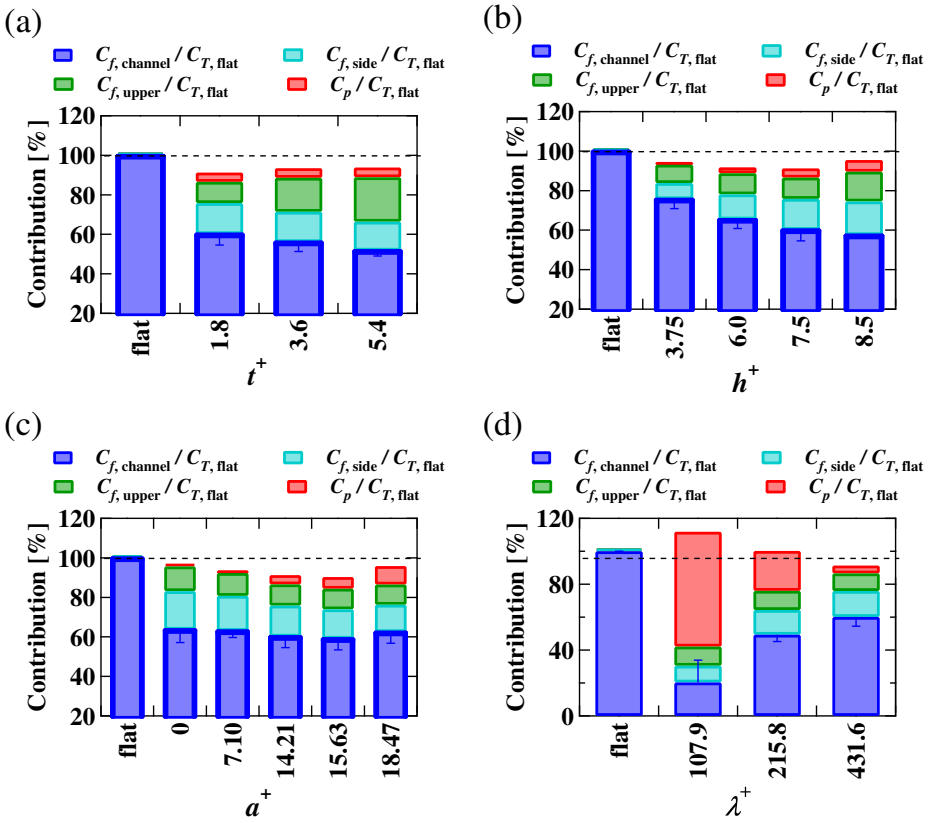


**Fig. 7** Drag reduction and contributions of each drag component with parameter variation: (a) thickness  $t^+$  ( $h^+ = 7.5$ ,  $a^+ = 14.22$ , and  $\lambda^+ = 431.6$ ); (b) height  $h^+$  ( $t^+ = 1.8$ ,  $a^+ = 14.22$ , and  $\lambda^+ = 431.6$ ) (c) amplitude  $a^+$  ( $h^+ = 7.5$ ,  $t^+ = 1.8$  and  $\lambda^+ = 431.6$ ) (d) wavelength  $\lambda^+$  ( $h^+ = 7.5$ ,  $t^+ = 1.8$ , and  $a^+ = 14.22$ )

the thickness and height increase, contributions from the upper and side walls of the riblet increase as shown in Fig. 7a–b. The pressure drag increases significantly in the cases of increased height or amplitude or decreased wavelength. In particular, when the wavelength is small ( $\lambda^+ \leq 215.8$ ), the pressure drag increases drastically since flow separation occurs.

According to Table 2 and Fig. 7, the sinusoidal riblet provided a drag reduction of 9.8% for the parameter set involving height  $h^+ = 7.5$ , thickness  $t^+ = 1.8$ , amplitude  $a^+ = 15.63$ , wavelength  $\lambda^+ = 431.6$ , and averaged lateral spacing  $s_{ave}^+ = 42.27$ . Even though the uncertainty of the drag reduction is  $\pm 2\%$ , as mentioned before, the optimal values of the height and amplitude are in the range of  $t^+ < 8.5$  and  $14.21 < a^+ < 18.47$ , respectively.

In the blade-type 2-D riblet, the optimal parameter sets is  $t^+ = 0.36$ ,  $h^+ = 9$ , and  $s^+ = 18$ , i.e., the thickness of the optimal 2-D riblet [2] is thinner than that of the sinusoidal riblet. In accordance, the thinner thickness of the sinusoidal riblet wall might be more effective in reducing the skin-friction drag. It is found that the height of the sinusoidal riblet is similar to that of a 2-D riblet. Previous studies with the 2-D riblet (e.g., [2, 4]) also reported that the drag reduction decreases when lateral spacing is larger than 25 wall units, which is a similar

value to the diameter of a quasi-streamwise vortex. On the other hand, the sinusoidal riblet has a drag reduction effect even if the average lateral spacing is large.

Additionally, we compare the sinusoidal riblet surface with the wall-oscillation control technique. The wall-oscillation technique is one of the active control techniques to decrease the skin-friction drag in wall turbulence (e.g., [32]). For example, Jung et al. [33] made the DNS of the turbulent channel flow with the temporally periodic spanwise wall oscillation as,

$$w = a \sin(2\pi/Tt). \quad (8)$$

Here,  $a$  and  $T$  denote the amplitude and period of the wall oscillation, respectively. They revealed that the optimal period was  $T^+ \approx 100$ , which corresponds streamwise length of  $\lambda^+ = 850$  in the present sinusoidal riblet. The present study shows, however, that the optimal amplitude and wavelength of the sinusoidal riblet surface are  $a^+ = 15$  and  $\lambda^+ = 341$ , respectively (it corresponds  $T^+ = 40$ ). Although the optimal parameters are comparable between of the wall-oscillation technique and the sinusoidal riblet, these flow fields cannot be straightforwardly compared due to twofold reasons: the spanwise velocity induced by the sinusoidal riblet is smaller than that by the wall oscillation (the maximum spanwise velocity in the sinusoidal riblet surface is 0.1 in wall unit); the sinusoidal riblet walls are out-of-phase and the spanwise velocity averaged in the spanwise direction should be zero.

## 4 Characteristic Flow

An important feature of the sinusoidal riblet is the streamwise variation of the lateral spacing of adjacent walls. Figure 8 shows the mean velocity distribution on the  $x$ - $z$  plane at  $y^+ = 7.5$ . Note that this height corresponds to the riblet wall height of  $h^+ = 7.5$ . The lateral spacing of the riblet expands at  $0 < x^+ < 216$  and contracts at  $216 < x^+ < 432$ . The streamwise velocity  $u^+$  and the wall-normal velocity  $v^+$  gradually vary in the streamwise direction and the flow generates non-zero Reynolds shear stress,  $-u^+v^+$ . The regions of the negative and positive spanwise velocity  $w^+$  are also observed. Hereafter, we refer to the upward and downward flows close to the riblet surface as the “characteristic flows”. The characteristic flow is confirmed by means of the PIV measurement [24, 25].

## 5 Turbulent Statistics

Before presenting turbulence statistics, we discuss the apparent origin of the wall-normal coordinates and define the “channel half-width.” Conventional study defines the apparent origin, since the wall surface is not flat and the origin of the wall-normal coordinate for statistics is not uniquely determined. For example, in the 2-D riblet surface case, Bechert et al. [6] defined the apparent origin by using viscous flow theory and Choi et al. [11] defined it at the peak of the turbulent kinetic energy ( $y^+ = 13$ ). In contrast to the 2-D riblet, these definitions of the virtual origin cannot be applied straightforwardly in the sinusoidal riblet because the lateral spacing of the riblet walls varies in the streamwise direction. Chan et al. [34] proposed some definitions for the virtual origin and one with the total shear balance arrived at the hydraulic radius (their study is for the pipe flow with roughness wall). Our previous study [24] of a sinusoidal riblet defined the origin of the wall-normal coordinate on the surface of the lower channel wall because “the channel half-width”  $\delta_{\text{rib}}$  in the riblet case is comparable with  $\delta$  (the distance between the channel walls in the flat surface

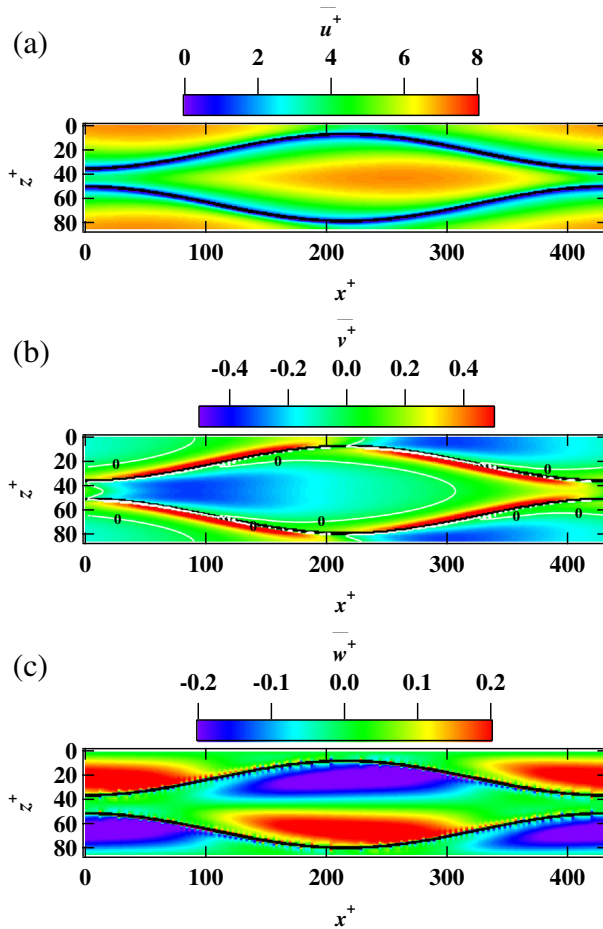


**Fig. 8** Distribution of the mean velocity of (a) streamwise, (b) wall-normal, and (c) spanwise components at  $y^+ = 7.5$

case). Here,  $\delta_{\text{rib}}$  is calculated from the cross-sectional area and the wetted perimeter. Moreover, the hydraulic height of the reference riblet case is  $\delta_h^+ = 109.687$  and the difference between  $\delta_h^+$  and  $\delta$  is 0.28%. Therefore, the present study also did not define the apparent origin and  $\delta$  is used as the reference length.

Figure 9 shows the streamwise velocity averaged in time and over the wall parallel plane at each wall normal height except for the riblet. Here, the streamwise mean velocity profiles near the wall apart from the linear law in the viscous sublayer, since the mean velocity is affected by the pressure drag and the riblet walls in the region close to the channel wall. As discussed in Eq. 5 and Fig. 7, the total shear balance consists of not only skin-friction drag of the channel wall, but also the pressure and skin-friction drag due to the riblet. Figure 9a shows the dependence on the thickness  $t^+$ ; a major dependence is not observed. The velocity is larger in the outer layer and smaller in the inner layer compared with velocities in the flat case. The increase of velocity in the outer layer corresponds to skin friction drag reduction because the mean pressure gradient is kept constant. On the other hand, the decrease

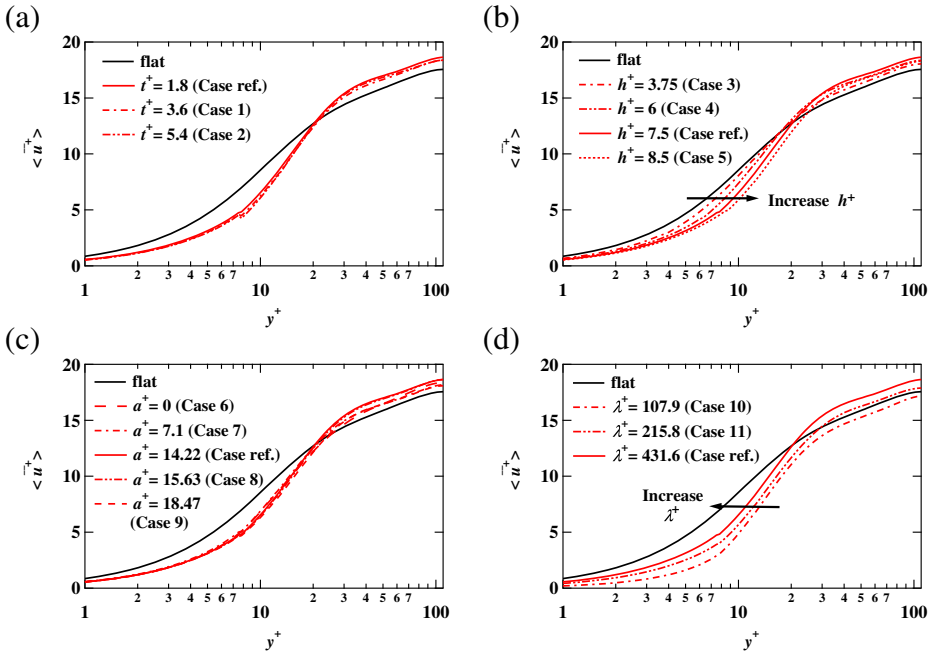


**Fig. 9** Dependence of the streamwise velocity on a single parameter: (a)  $t^+$ ; (b)  $h^+$ ; (c)  $a^+$ ; and (d)  $\lambda^+$

of velocity in the inner layer implies the reduction of the wall shear stress. This trend is common for the other parameter cases, as shown in Fig. 9b–c, and for the 2-D riblet surface [1, 4, 11]. The dependence on the height  $h^+$  is depicted in Fig. 9b. The velocity in the case of the reference shape is largest in the outer layer and  $h^+$  is optimal for drag reduction. Figure 9c displays the dependence on amplitude  $a^+$ . The velocities in the inner layer are almost unchanged for different amplitudes while those in the case of the reference shape and in Case 8 are larger than in the outer layer. The effect of the wavelength is shown in Fig. 9d. The velocity in the shorter-wavelength case decreases not only in the inner layer, but also in the outer layer. This is because of flow separation which tends to occur in the shorter-wavelength case.

In order to clarify the effect of the characteristic flow generated by the sinusoidal riblet on the Reynolds shear stress (henceforth referred to as RSS), we employ a three-component decomposition defined as

$$u_i = \langle \bar{u}_i \rangle + \tilde{u}_i + u_i'' \tag{9}$$

The instantaneous velocity  $u_i$  is decomposed into a mean component  $\langle \bar{u}_i \rangle$ , a periodic component  $\tilde{u}_i$ , and a random component,  $u_i''$ . The averaging procedure is as follows:

$$\langle \bar{u}_i \rangle(y) = \frac{1}{ST} \int_S \int_T u_i(x, y, z, t) dt ds, \tag{10}$$

$$\tilde{u}_i(x, y, z) = \bar{u}_i(x, y, z) - \langle \bar{u}_i \rangle(y), \tag{11}$$

$$u_i''(x, y, z, t) = u_i(x, y, z, t) - \bar{u}_i(x, y, z). \tag{12}$$

The periodic component  $\tilde{u}_i$  is the difference between the time-averaged component  $\overline{u_i}$  and the spatio-temporally averaged component  $\langle \overline{u_i} \rangle$ . Here,  $S$  is the area of the  $x - y$  plane except for the riblet and  $ds$  is its element area. The bar indicates a value averaged over the time duration  $T$ . According to the three-component decomposition, the decomposed RSS is

$$-\overline{u'^+v'^+} = -\overline{\tilde{u}^+\tilde{v}^+} - \overline{u''^+v''^+}. \tag{13}$$

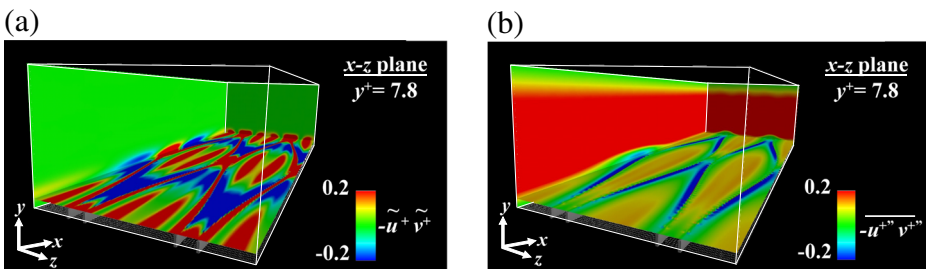
Here, the correlation between the random and periodic velocities (e.g.,  $\overline{\tilde{u}\tilde{v}}$ ) is negligibly small. We refer to the first and second terms on the RHS as ‘periodic’ and ‘random’ components, respectively.

Figure 10 shows the distribution of  $-\overline{\tilde{u}^+\tilde{v}^+}$  and  $-\overline{u''^+v''^+}$  on the  $x - z$  plane at  $y^+ = 7.8$  in the case of the reference shape. The negative and positive  $-\overline{\tilde{u}^+\tilde{v}^+}$  are observed in Fig. 10a, which is generated by the characteristic flow. On the other hand,  $-\overline{u''^+v''^+}$  is positive and its value is uniform away from the wall although it is slightly negative close to the riblet wall. In the following discussion, we show the profiles of  $-\overline{\tilde{u}^+\tilde{v}^+}$  and  $-\overline{u''^+v''^+}$  averaged on the  $x - z$  plane, and we refer to them as the periodic and random RSS, respectively.

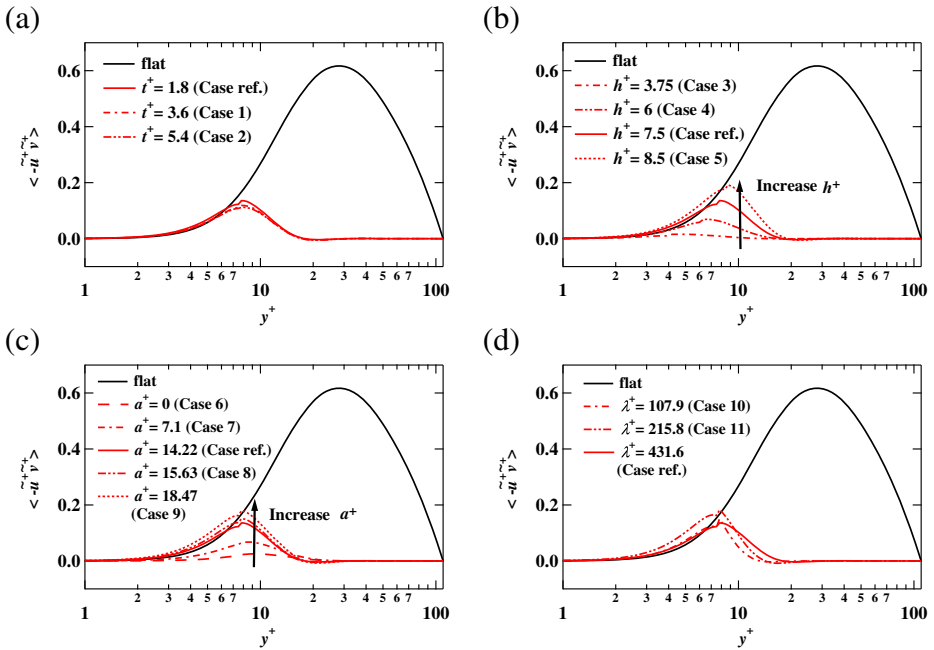
Figure 11 shows the spatio-temporally averaged periodic RSS and its dependence on individual parameters. The RSS in the flat case is also shown here for comparison (the ‘‘periodic RSS’’ is absent). The positive periodic RSS appears close to the wall and is unchanged for different  $t^+$ , as shown in Fig. 11a. With increasing  $h^+$  and  $a^+$ , the periodic RSS increases as shown in Fig. 11b and c. Note that the periodic RSS in the case of the straight riblet (Case 6) shows a different profile from the others because the characteristic flows are not generated. The positive periodic RSS is also generated for different wavelength cases. Roughly speaking, the periodic RSS induced by the characteristic flows is positive in the region near the wall, and this contributes to increasing the skin friction drag.

Figure 12a shows the random RSS for different  $t^+$ . The dependence on  $t^+$  is small. As compared with the flat case, the random RSS decreases and its peak shifts away from the wall and decreases. This implies that the riblet attenuates the intensity of vortical structures since the random RSS corresponds to turbulence, described later in Section 6. On the other hand, with increasing  $h^+$  and  $a^+$ , the random RSS decreases as shown in Fig. 12b and c. Figure 12d shows its dependence on  $\lambda^+$ . The negative random RSS appears at  $y^+ \approx 9$  where flow separation occurs in the shorter-wavelength case.

As compared between Figs. 11d and 12d, although the wavelengths are different, the random and periodic RSS are almost unchanged. To explain them, the random RSS distributions on the  $x - z$  plane are displayed in Fig. 13. In the Case ref., the random RSS gradually changes along to the riblet surface. In contrast, in the shorter wavelength case (Case 10), the maximum and minimum random RSS enlarges. These increment and decrement, however,



**Fig. 10** Distribution of (a)  $-\overline{\tilde{u}^+\tilde{v}^+}$  and (b)  $-\overline{u''^+v''^+}$  in the case of the reference shape. The  $x - z$  plane is at  $y^+ = 7.35$



**Fig. 11** Dependence of the periodic RSS on individual parameters: (a)  $t^+$ ; (b)  $h^+$ ; (c)  $a^+$ ; and (d)  $\lambda^+$

are canceled out and the averaged random RSS are similar with Case Ref. Since the pressure drag increases due to the short wavelength, the total drag increases (+12%) in the Case 10.

As a short summary, the results obtained show that the decrease of drag when using a sinusoidal riblet surface results from decreasing the random RSS rather than the periodic RSS. In our previous study [24], we performed pathline analysis and concluded that the characteristic flows inhibit quasi-streamwise vortices from approaching the channel wall. The periodic RSS would contribute indirectly to the decrease of the random RSS. In the next section, we present vortex tracking to discuss the drag reduction mechanism as an extension of the previous pathline analysis.

### 6 Tracking of Vortical Structures

In wall turbulence, quasi-streamwise vortical structures exchange momentum between the regions near the wall and away from the wall and sustain high skin friction drag. The quasi-streamwise vortical structures are often identified by using the second invariant of the velocity deformation tensor: the so-called  $Q$  value (e.g., Kasagi et al. [35]) defined as

$$Q = s'_{ij}s'_{ij} - \omega'_{ij}\omega'_{ij}, \tag{14}$$

where  $s'_{ij}$  and  $\omega'_{ij}$  are the symmetric and asymmetric parts of the deformation tensor, respectively. Figure 14 visualizes the vortical structure ( $Q^+ = -0.04$ ) in the lower half of the channel in the flat and the reference shape cases. The vortical structure is observed in both cases while no major difference is obtained.

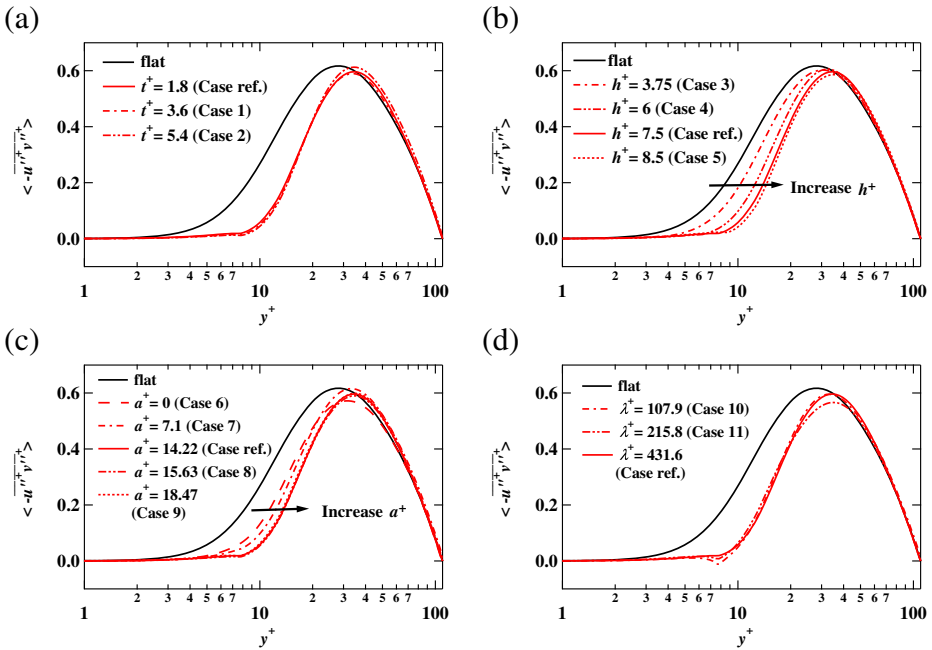


**Fig. 12** Dependence of the random RSS on individual parameters: (a)  $t^+$ ; (b)  $h^+$ ; (c)  $a^+$ ; and (d)  $\lambda^+$

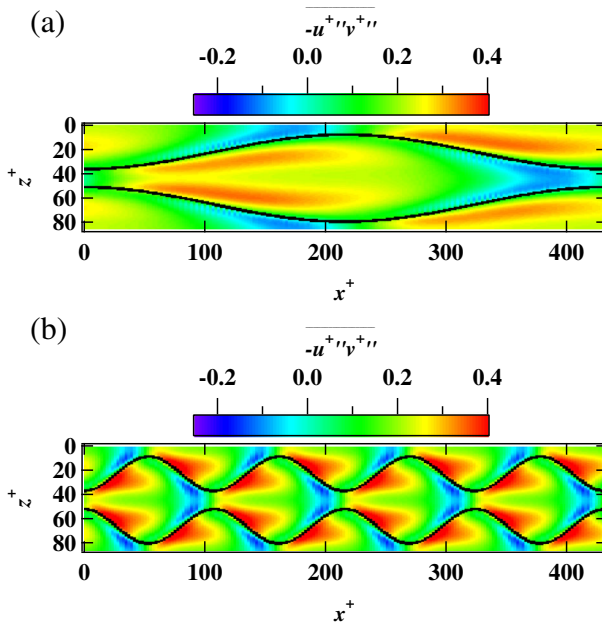
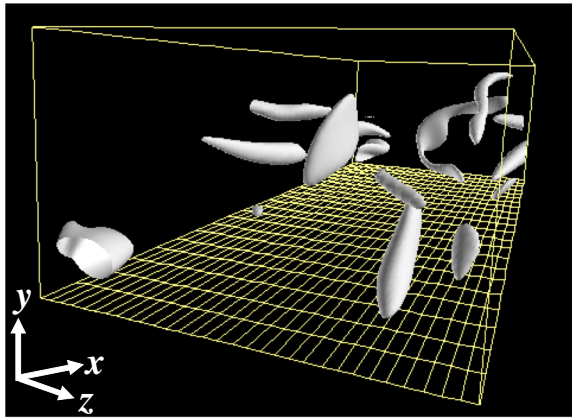


**Fig. 13** Distributions of random RSS over the riblet surface at  $y^+ = 13$ ; (a) Reference (max, 0.34; min, -0.11), (b)  $\lambda^+ = 107.9$  (Case 10) (max, 0.44; min, -0.46)



(a)



(b)

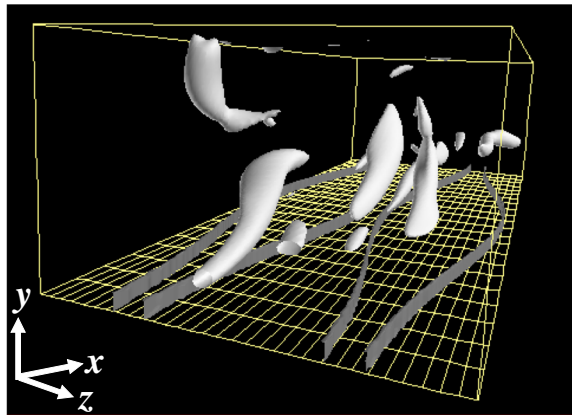


**Fig. 14** Visualization of instantaneous flow fields in the flat case and the reference shape case. The *white color* represents an isosurface of  $Q^+ = -0.04$

In order to quantify the vortical structure, we extract its core using the following procedure:

- set the threshold value  $Q^+ = -0.04$  and count the region of  $Q^+ \leq -0.04$  as “the vortical structure”;
- define the position of negative and minimum  $Q^+$  in the vortical structure as “the core.”

Figure 15 shows the distribution of the averaged  $Q$  value of the core in the flat and reference shape cases. Here, we divide the computational domain into 1024 cells to average the  $Q$  value of the core: the cells are located at  $0 < y^+ < 50$ ; the streamwise and spanwise widths of the cells are 18 and 0.1 in wall units, respectively. The averaged  $Q$  value of the core is almost uniform in the flat case as shown in Fig. 15a, whereas it is decreased in the reference shape case as shown Fig. 15b. Since vortical structures travel where the mean shear is reduced due to the riblet, the vortical structure and its  $Q$  value are attenuated. Locally, the

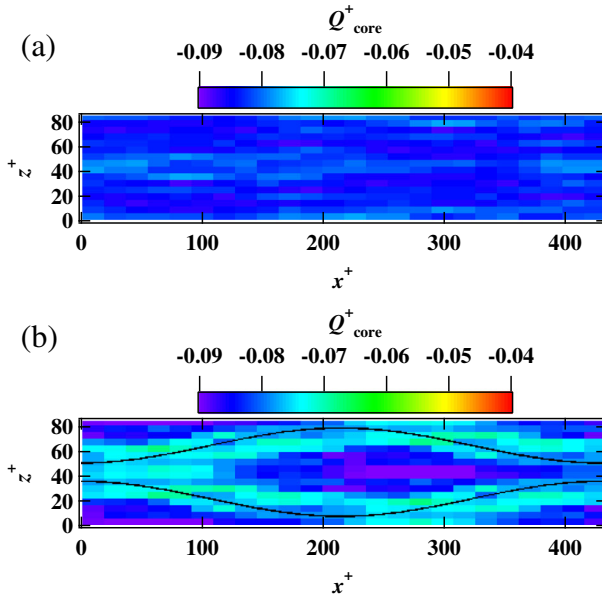


**Fig. 15** The averaged  $Q$  value of the core for the vortical structure in (a) the flat case and (b) the reference shape case

negative  $Q$  value of the core is strengthened in the contracted region of the riblet walls, corresponding to the large mean shear region as shown Fig. 16. This trend is common for flows over the sinusoidal riblet.

Our previous experiments [24–26] showed that the riblet prevents the vortex from hitting the wall; if the vortical structure approaches the wall due to the downward flow, it is shifted away from the wall due to the upward flow, where the investigation was conducted on the  $x$ - $y$  plane at the center of the adjacent walls of the riblet. In contrast to previous experiments, in the present work vortical structures are tracked directly in three-dimensional space by means of DNS.

The procedure of vortex tracking is explained in Fig. 17 and as follows:

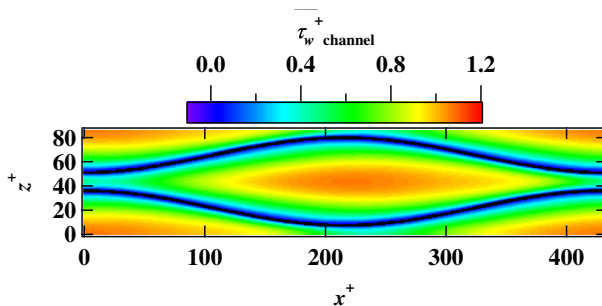


**Fig. 16** Wall shear stress on the channel lower wall for the reference shape case

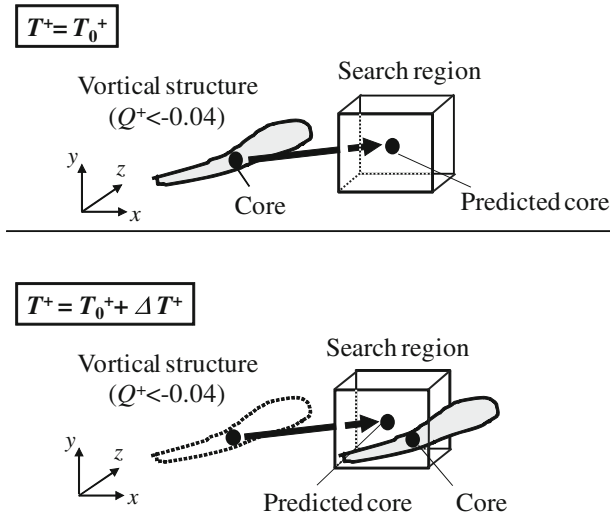


Fig. 17 Schematic of vortex tracking

- set the threshold value of  $Q^+ = -0.04$  and count the region of  $Q^+ \leq -0.04$  as “the vortical structure”;
- calculate the minimum  $Q^+$  of the vortical structure and consider it as “the core”;
- interpolate the position of “the core” with second sub-grid interpolation;
- predict the core position in the next time step (called the “predicted core”) using the local velocity at the present core position;
- define the “search area” centering on the predicted core, where the width and height of the search area are  $3u_{RMS}^+(x, y, z) \times \Delta T^+$ ,  $3v_{RMS}^+(x, y, z) \times \Delta T^+$ , and  $3w_{RMS}^+(x, y, z) \times \Delta T^+$ , respectively;
- use the flow field in the next time step image (i.e.,  $T^+ = T_0^+ + \Delta T^+$ ) and calculate the core position;
- calculate the advection distance of the vortical structure if the core exists in the search region.

In order to maintain consistency with previous studies, we evaluate the displacement of the vortical structure in the wall-normal direction and discuss the probability of wall-normal displacement of the vortical structure. Here, we introduce the counter  $I$  defined in each cell: with  $I_{up,i} = 1$  and  $I_{down,i} = 0$ , the core of the vortical structure shifts upward;  $I_{up,i} = 0$  and  $I_{down,i} = 1$  if the vortical structure moves toward the wall. The subscript  $i$  denotes the order of the velocity field. Thus, the probability function is introduced as

$$P_{up} = \frac{\sum_i I_{up,i}}{\sum (I_{down,i} + I_{up,i})}, \tag{15}$$

$$P_{down} = \frac{\sum_i I_{down,i}}{\sum (I_{down,i} + I_{up,i})}. \tag{16}$$

Here,  $P_{up}$  and  $P_{down}$  denote the probability of the vortical structure leaving the wall and moving toward the wall, respectively. The sum of  $P_{up}$  and  $P_{down}$  equals one.

Figure 18 shows the probability,  $P_{up}$  and  $P_{down}$  in the reference shape case. The results are averaged within the same cell for Fig. 15. If the wall is the flat, the probability of  $P_{down}$

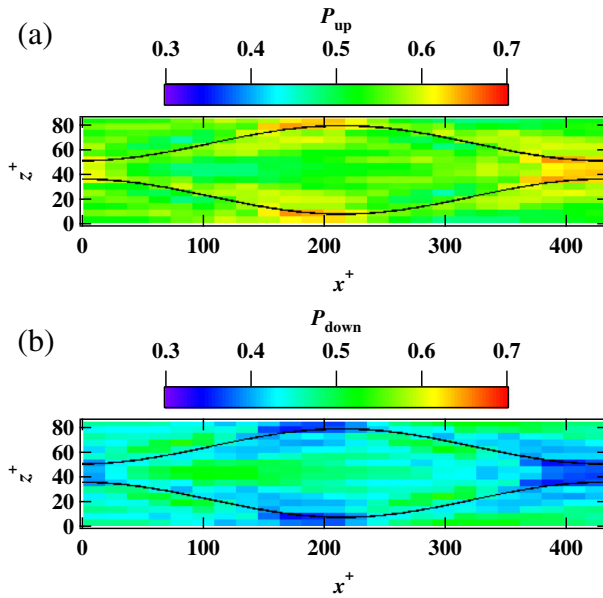


**Fig. 18** Probability of the sign of vortex displacement in the wall-normal direction in the case of reference: (a) positive displacement and (b) negative displacement

and  $P_{up}$  are 0.5. In the riblet case,  $P_{up}$  is smaller and  $P_{down}$  is larger than 0.5 in the expanding region of  $50 < x^+ < 150$ , indicating that the vortical structure approaches the wall owing to the downward flow. In the region where the riblet spacing is narrow,  $P_{up}$  is larger and  $P_{down}$  is smaller than 0.5. Therefore, the vortical structure leaves the near-wall region where the upward flow occurs, which supports experimental results by Yamaguchi et al. [25, 26].

To clarify this, Fig. 19 shows the probability function on the  $x - y$  plane at the center of the riblet walls. The solid and broken lines are  $P_{up}$  and  $P_{down}$ , respectively. Similar to the observation in Fig. 18, variation of  $P_{up}$  and  $P_{down}$  is observed in the streamwise direction. Figure 20 shows variation of the average height and the  $Q$  value of the core on the center

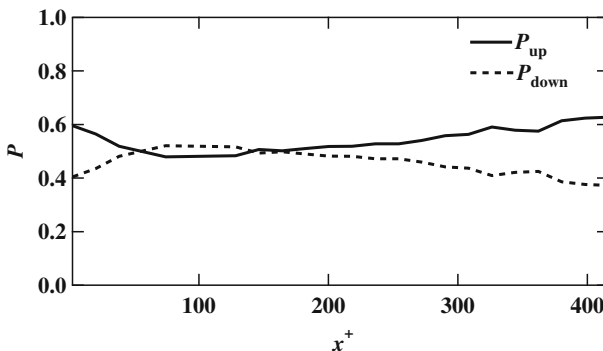


**Fig. 19** Probability of the sign of vortex displacement in the wall-normal direction at the center between riblet walls in the reference shape case

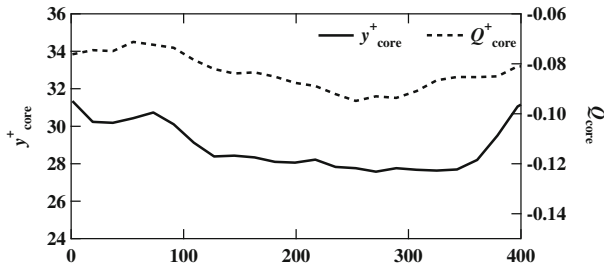


**Fig. 20** Average height of the core and intensity of the core at the center between riblet walls in the reference shape case

plane of the riblet walls. The average height and its  $Q$  value decrease in the expanding region and increase in the contracting region of the riblet walls, which implies that the vortical structure follows the characteristic flow.

From above, the mechanism of the drag reduction by the present sinusoidal riblet surface can be stated. Due to the sinusoidal riblet, vortical structures are attenuated. Even if vortical structures approach the wall due to the downward motion of the characteristic flow, the high wall-shear stress region is localized at the expanded region of the riblet walls. In consequence, the wetted area of the sinusoidal riblet is smaller than that of the 2-D riblet, resulting in the drag-reduction effect. This discussion is in accordance with our previous experimental studies [24, 25].

## 7 Conclusions

The direct numerical simulation of fully developed turbulent channel flow with the sinusoidal riblet surface has been performed at a friction Reynolds number of 110. The sinusoidal riblet involves lateral spacing between walls that varies sinusoidally in the streamwise direction and wetted area that is smaller than for ordinary, straight-type riblets. A drag reduction effect when using the sinusoidal riblet was found by means of our previous experimental studies. As an extension, we investigated the effect of the design parameters of the sinusoidal riblet on the drag reduction rate and flow statistics in this paper. We also performed vortex tracking to discuss the motion of the vortical structure traveling over the sinusoidal riblet surface.

1. Due to the sinusoidal riblet surface, the skin friction on the channel wall drastically decreased while other contributions appear (the skin friction on the side and top walls of the riblet and the pressure drag).
2. Maximum drag reduction of  $9.8\% \pm 2\%$  was obtained at a thickness of  $t^+ = 1.8$ , height of  $h^+ = 7.5$ , wavelength of  $\lambda^+ = 431.6$ , amplitude of  $a^+ = 14.22$ , and average lateral spacing of  $s_{\text{ave}}^+ = 42.27$ .
3. The sinusoidal riblet surface generated a characteristic flow: upward and downward flows where lateral spacing expands or contracts, respectively.
4. The dependence of the thickness  $t^+$  on the flow statistics was small.
5. As the height  $h^+$  and amplitude  $a^+$  of the sinusoidal riblet increased, the periodic RSS increased while the random RSS decreased.

6. In the shorter-wavelength case, the skin friction drag decreased and the pressure drag increased owing to flow separation, increasing the total drag.
7. The vortex tracking and the probability analysis for the core of the vortical structure showed that the vortical structure was attenuated owing to the sinusoidal riblet and followed the characteristic flows. Even if the vortical structure approaches the wall, it leaves the wall due to the induced upward flow.
8. Due to the sinusoidal riblet, vortical structures are attenuated and the high wall-shear stress region on the channel wall is localized. In consequence, the wetted area of the sinusoidal riblet is small and we obtain the drag-reduction effect owing to the sinusoidal riblet.

**Acknowledgments** This research was partially supported by the Ministry of Education, Culture, Sports, Science and Technology through a Grant-in-Aid for Scientific Research (C) of 15K05785 in 2015. This work was also partially supported by Council for Science, Technology and Innovation (CSTI), Cross-ministerial Strategic Innovation Promotion Program (SIP), “Innovative Combustion Technology” (Funding agency: JST). The authors acknowledge their co-worker, Mr. Makoto Serizawa.

## References

1. Walsh, M.J.: Turbulent boundary layer drag reduction using riblets. *Amer. Inst. Aeronaut. Astronaut.* (AIAA-paper 82–0169), p. 8 (1982)
2. Bechert, D., Bruse, M., Hage, W., Van der Hoeven, J.T., Hoppe, G.: Experiments on drag-reducing surfaces and their optimization with an adjustable geometry. *J. Fluid Mech.* **338**, 59–87 (1997)
3. Choi, K.S.: Near-wall structure of a turbulent boundary layer with riblets. *J. Fluid Mech.* **208**, 417–458 (1989)
4. El-Samni, O., Chun, H., Yoon, H.: Drag reduction of turbulent flow over thin rectangular riblets. *Int. J. Eng. Sci.* **45**(2), 436–454 (2007)
5. Walsh, M.J.: Riblets as a viscous drag reduction technique. *Amer. Inst. Aeronaut. Astronaut.* **21**, 485–486 (1983)
6. Bechert, D., Bartenwerfer, M.: The viscous flow on surfaces with longitudinal ribs. *J. Fluid Mech.* **206**, 105–129 (1989)
7. Luchini, P., Manzo, F., Pozzi, A.: Resistance of a grooved surface to parallel flow and cross-flow. *J. Fluid Mech.* **228**, 87–109 (1991)
8. Mayoral, G.R., Jiménez, J.: Hydrodynamic stability and breakdown of the viscous regime over riblets. *J. Fluid Mech.* **678**, 317–347 (2011)
9. Lee, S.J., Lee, S.H.: Flow field analysis of a turbulent boundary layer over a riblet surface. *Exp. Fluids* **30**(2), 153–166 (2001)
10. Suzuki, Y., Yoshino, T., Yamagami, T., Kasagi, N.: Drag reduction in a turbulent channel flow by using a ga-based feedback control system. In: *Proc. 6th Symp. Smart Control of Turbulence*, pp. 31–40 (2005)
11. Choi, H., Moin, P., Kim, J.: Direct numerical simulation of turbulent flow over riblets. *J. Fluid Mech.* **225**, 503–539 (1993)
12. Chu, D., Karniadakis, G.: A direct numerical simulation of laminar and turbulent flow over riblet-mounted surfaces. *J. Fluid Mech.* **250**, 1–42 (1993)
13. Goldstein, D., Handler, R., Sirovich, L.: Direct numerical simulation of turbulent flow over a modeled riblet covered surface. *J. Fluid Mech.* **302**, 333–376 (1995)
14. Viswanath, P.: Aircraft viscous drag reduction using riblets. *Progress Aerosp. Sci.* **38**(6), 571–600 (2002)
15. Bechert, D., Bruse, M., Hage, W.: Experiments with three-dimensional riblets as an idealized model of shark skin. *Exp. Fluids* **28**(5), 403–412 (2000)
16. Peet, Y., Sagaut, P.: Theoretical prediction of turbulent skin friction on geometrically complex surfaces. *Phys. Fluids* **21**(105105), 19 (2009)
17. Peet, Y., Sagaut, P., Charron, Y.: Turbulent drag reduction using sinusoidal riblets with triangular cross-section. In: *The 38th AIAA Fluid Dynamics Conference and Exhibit (AIAA-2008-3745)*, p. 9 (2008)
18. Chen, H., Rao, F., Shang, X., Zhang, D., Hagiwara, I.: Biomimetic drag reduction study on herringbone riblets of bird feather. *J. Bionic Eng.* **10**, 341–349 (2013)

19. Berger, T.W., Kim, J., Lee, C., Lim, J.: Turbulent boundary layer control utilizing the lorentz force. *Phys. Fluids* **12**, 631–649 (2000)
20. Choi, K.S., Graham, M.: Drag reduction of turbulent pipe flows by circular-wall oscillation. *Phys. Fluids* **10**(1), 7–9 (1998)
21. Jung, W.J., Mangiavacchi, N., Akhavan, R.: Suppression of turbulence in wall-bounded flows by high-frequency spanwise oscillations. *Phys. Fluids A* **4**, 1605–1607 (1992)
22. Sha, T., Itoh, M., Tamano, S., Akino, N.: Experimental study on drag reduction in turbulent flow on zigzag riblet surface. In: The 88th Fluid Engineering Division Conference of the Japan Society of Mechanical Engineers, vol. 207, pp. 21. (in Japanese), <http://ci.nii.ac.jp/naid/110006207871> (2005)
23. Viotti, C., Quadrio, M., Luchini, P.: Streamwise oscillation of spanwise velocity at the wall of a channel for turbulent drag reduction. *Phys. Fluids* **21**(115), 109 (2009)
24. Sasamori, M., Mamori, H., Iwamoto, K., Murata, A.: Experimental study on drag-reduction effect due to sinusoidal riblets in turbulent channel flow. *Exp. Fluids* **55**, 1–14 (2014)
25. Mamori, H., Yamaguchi, K., Sasamori, M., Iwamoto, K., Murata, A.: Analysis of vortical structure over sinusoidal riblet surface in turbulent channel flow by means of Dual-plane stereoscopic PIV measurement. In: The 69th Annual Meeting of the APS Division of Fluid Dynamics (Abstract:H7.00004) (2016)
26. Yamaguchi, K., Sasamori, M., Mamori, H., Iwamoto, K., Murata, A.: Analysis of vortical structure over a sinusoidal riblet by dual-plane stereoscopic PIV. In: Proc. of International Symposium on Application of Laser Techniques to Fluid Mechanics Lisbon, vol. 119, p. 7 (2014)
27. Kim, J., Kim, D., Choi, H.: An immersed-boundary finite-volume method for simulations of flow in complex geometries. *J. Comput. Phys.* **171**, 132–150 (2001)
28. Spalart, P.R., MaLean, J.D.: Drag reduction: enticing turbulence, and then an industry. *Phil. Trans. R. Soc. A* **369**, 1556–1569 (2011)
29. Iwamoto, K., Fukagata, K., Kasagi, N., Suzuki, Y.: Friction drag reduction achievable by near-wall turbulence manipulation at high reynolds numbers. *Phys. Fluids* **17**(011702), 4 (2005)
30. Garcia-Mayoral, R., Jimenez, J.: Drag reduction by riblets. *Phil. Trans. R. Soc. A* **369**, 1412–1427 (2011)
31. Iwamoto, K., Suzuki, Y., Kasagi, N.: Reynolds number effect on wall turbulence: Toward effective feedback control. *Int. J. Heat Fluid Flow* **23**, 678–689 (2002)
32. Karniadakis, G., Choi, K.S.: Mechanisms on transverse motions in turbulent wall flows. *Annu. Rev. Fluid Mech.* **35**(1), 45–62 (2003)
33. Jung, W., Mangiavacchi, N., Akhavan, R.: Suppression of turbulence in wall-bounded flows by high-frequency spanwise oscillations. *Phys. Fluids A: Fluid Dyn. (1989–1993)* **4**(8), 1605–1607 (1992)
34. Chan, L., MacDonald, M., Chung, D., Hutchins, Ooi, A.: A systematic investigation of roughness height and wavelength in turbulent pipe flow in the transitionally rough regime. *J. Fluid Mech.* **771**, 743–777 (2015)
35. Kasagi, N., Sumitani, Y., Suzuki, Y., Iida, O.: Kinematics of the quasi-coherent vortical structure in near-wall turbulence. *Int. J. Heat Fluid Flow* **16**(1), 2–10 (1995)